The Astrophysical Journal, 820:91 (10pp), 2016 April 1 doi:10.3847/0004-637X/820/2/91

AN ADJOINT-BASED METHOD FOR THE INVERSION OF THE *JUNO* AND *CASSINI* GRAVITY MEASUREMENTS INTO WIND FIELDS

Eli Galanti and Yohai Kaspi
Weizmann Institute of Science, Rehovot, Israel; eli.galanti@weizmann.ac.il
Received 2015 August 19; accepted 2016 January 6; published 2016 March 22

ABSTRACT

During 2016–17, the *Juno* and *Cassini* spacecraft will both perform close eccentric orbits of Jupiter and Saturn, respectively, obtaining high-precision gravity measurements for these planets. These data will be used to estimate the depth of the observed surface flows on these planets. All models to date, relating the winds to the gravity field, have been in the forward direction, thus only allowing the calculation of the gravity field from given wind models. However, there is a need to do the inverse problem since the new observations will be of the gravity field. Here, an inverse dynamical model is developed to relate the expected measurable gravity field, to perturbations of the density and wind fields, and therefore to the observed cloud-level winds. In order to invert the gravity field into the 3D circulation, an adjoint model is constructed for the dynamical model, thus allowing backward integration. This tool is used for the examination of various scenarios, simulating cases in which the depth of the wind depends on latitude. We show that it is possible to use the gravity measurements to derive the depth of the winds, both on Jupiter and Saturn, also taking into account measurement errors. Calculating the solution uncertainties, we show that the wind depth can be determined more precisely in the low-to-mid-latitudes. In addition, the gravitational moments are found to be particularly sensitive to flows at the equatorial intermediate depths. Therefore, we expect that if deep winds exist on these planets they will have a measurable signature by *Juno* and *Cassini*.

Key words: gravitation – hydrodynamics – planets and satellites: atmospheres – planets and satellites: gaseous planets

1. INTRODUCTION

At the observed cloud level of both Jupiter and Saturn, atmospheric dynamics are dominated by strong east–west (zonal) jet streams (Figure 1), reaching velocities of 140 ms^{-1} on Jupiter and over 400 ms^{-1} on Saturn (Vasavada & Showman 2005). It is currently unknown how deep these jets extend (e.g., Li et al. 2006; Del Genio & Barbara 2012), and the only available direct measurements below the cloud-level are from the 1995 Galileo probe to Jupiter that found 160 ms^{-1} winds extending down to at least 22 bars at the entry point of the probe (6°N; Atkinson et al. 1996). Addressing this question is one of the main goals of the *Juno* mission to Jupiter and of the *Cassini* proximal orbits around Saturn. Their aim is to determine the depth extent of atmospheric circulation on these planets through precise measurements of their gravity field (Hubbard 1999; Kaspi et al. 2010). This may allow us to answer the long lasting debate regarding the depth of the dynamics on giant planets, and thus shed light on the mechanisms the could be driving the jets (e.g., Busse 1976; Williams 1978; Cho & Polvani 1996; Showman et al. 2006; Kaspi & Flierl 2007; Scott & Polvani 2007; Lian & Showman 2010; Liu & Schneider 2010; Liu et al. 2013).

The *Juno* mission was launched in 2011 and will arrive at Jupiter in 2016 equipped to perform high-precision measurements of the gravity field with expected accuracy that will allow meaningful measurements up to at least J_{12} (Bolton 2005). In 2017, NASA's *Cassini* mission will conclude its 13-year tour of the Saturnian system, with planned proximal orbits of Saturn obtaining the same type of data for Saturn, just before the spacecraft terminates its operation by descending into Saturn's interior. For both spacecraft, the detection of the gravity signal will be done by Doppler tracking of the spacecraft trajectory.

In recent years, in anticipation of the arrival of *Juno* at Jupiter, several studies have looked at the effect of interior flow on the gravitational signature of the planet. To leading order, the gravity spectrum is affected by the planet's oblate shape and radial density distribution. However, on giant gas planets, since they are composed mainly of light elements and have no solid surface, the relative effect of density perturbations due to their internal and atmospheric dynamics can be significant and affect the measured gravity field. Particularly, if the strong winds extend deep enough into the planets' interior, their relative effect on gravity becomes larger. This was first noted by Hubbard (1982) and later developed further by Hubbard (1999). In these studies, potential theory (the adjustment of potential surfaces under rotational and internal structure constraints) was used to show that if differential rotation on Jupiter penetrates the depth of the planet, then the resulting high-order gravity moments will be stronger than the corresponding solid-body moments. This approach was recently further developed using more accurate concentric MacLaurin-based interior models (Hubbard 2012, 2013; Kong et al. 2012).

These studies have allowed accurate estimation of the gravity field, but have been limited to flows following full cylindrical symmetry because these potential theory models are limited to fully barotropic systems in which the flow is constant along lines parallel to the axis of rotation. A second approach proposed was using thermal wind balance models (Kaspi et al. 2010, 2013b; Kaspi 2013; Liu et al. 2013), where the gravity field resulting from any given wind field could be calculated; however, these models are limited to spherical symmetry, resulting in the inability to calculate the static (solid-body) gravity spectrum and neglecting the effect of the planet oblateness on the wind contribution to the gravity moments. Kong et al. (2012) calculated this effect for the case of the full

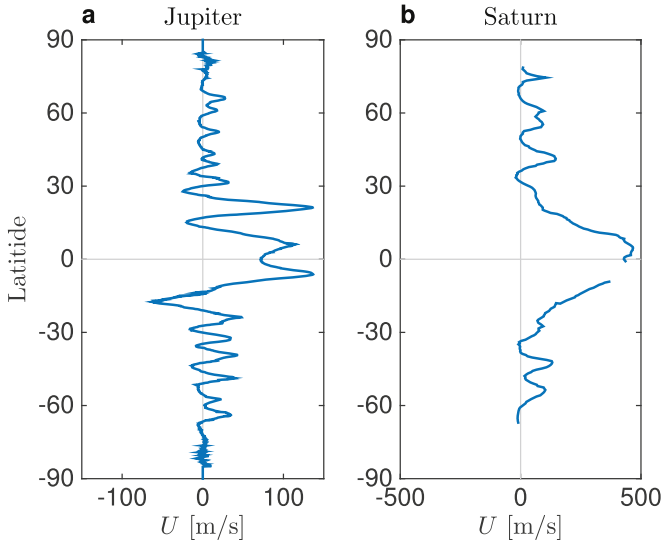

Figure 1. (a) Surface winds on Jupiter (Porco et al. 2003) and (b) surface winds on Saturn (Sanchez-Lavega et al. 2000).

barotropic flow, and found it to be small. Similarly, using a thermal-wind-based model with an oblate mean state density structure, we find that the effect of oblateness on the dynamical contribution to the gravity moments is small (Kaspi et al. 2013a, 2016).

Because Jupiter and Saturn are gaseous, aside from the cloud-level winds, there is no apparent asymmetry between the northern and southern hemispheres. Therefore, the gravitational moments resulting from the shape and vertical structure of the planets have identically zero odd moments (Kaspi 2013). However, the observed cloud-level wind structure does have hemispherical differences, and it was shown that, even if these asymmetries extend only $O(100)$ km below the surface, their contribution to the odd gravity moments is measurable (Kaspi 2013). Unlike the even moments that have a contribution both from the static density distribution and the dynamics, the odd moments are caused purely due to dynamics. Thus, any odd signal detected (J_3, J_5, J_7, …) will be a sign of a dynamical contribution to the gravity signal, and this might be one of the first signals of deep dynamics that might be measured by *Juno* and *Cassini*. Also using the thermal wind approach, Liu et al. (2013) calculated the penetration depth of the winds on Jupiter with the additional assumption that the entropy gradient in the direction of the spin axis must be zero. This requirement sets the penetration depth of the winds, and they have also found that such a wind structure should be detectable by *Juno* and *Cassini* (Liu et al. 2014).

All studies to date have been only in the direction of forward modeling; thus, given a hypothetical wind structure (based on the observed surface winds and some assumption regarding the penetration depth) the gravity moments are calculated via the effect of the winds on the density structure (e.g., Hubbard 1999; Kaspi et al. 2010; Kong et al. 2012; Liu et al. 2013). However, in order to analyze the gravity field that will be detected by *Juno* and *Cassini*, we need to solve the inverse problem, and calculate the zonal wind profile given the gravity field. This causes difficulty since a gravity field is not necessarily invertible, and a given gravity field might not have a unique corresponding wind structure. Here, we address this issue by proposing an adjoint based inverse method that will allow the investigation of the giant planet dynamics using the observed measured gravity field. This method has been used extensively in the study of oceanic and atmospheric fluid dynamics (e.g., Tziperman & Thacker 1989; Mazloff et al. 2010; Moore et al. 2011; Kalmikov & Heimbach 2014). In this study, we present results based on the zonal winds only, but this method will enable us to relate them to the full gravity maps, not only for the zonal moments, but for the full 3D gravity fields including contributions from longitudinal variations in the wind structure and meridional winds. These variations might be detectable if the depth of these longitudinal features have a depth of at least a few thousand kilometers (Parisi et al. 2016). Moreover, the adjoint model we present in this study is derived using the forward model based on the thermal wind method. However, the inversion method is more general and can be applied to more complex models (e.g., Zhang et al. 2015) or general circulation models as is often done in ocean science (e.g., Galanti et al. 2003; Mazloff et al. 2010).

In Section 2, we describe the thermal wind forward method for calculating the wind induced contribution to the gravity moments, its adjoint counterpart, and the optimization procedure used to find the depth of the winds. In Section 3, we discuss the results for several cases, a case with wind depth that is not varying with latitude, a case where the wind depth on Jupiter is allowed to vary with latitude, and the same analysis applied for Saturn. We also discuss sensitivities to flow perturbations in the planet deep interior. We discuss the results and their implications for the *Juno* and *Cassini* missions in Section 4.

2. METHODS

The relation between the density structure of the planet and the resulting gravity signature can be interpreted using the zonal gravity moments, which are defined as

$$J_n = -\frac{1}{Ma^n}\int P_n \rho r^n d^3\mathbf{r}, \quad (1)$$

where M is the planetary mass, a is the mean planetary radius, P_n is the nth Legendre polynomial, and ρ is the local density (Hubbard 1984). The density can be divided into the solid-body component $\tilde{\rho}(r, \theta)$, and a dynamical component $\rho'(r, \theta)$ arising from the fluid motion (θ is latitude), so that $\rho = \tilde{\rho} + \rho'$ (see Kaspi 2013 for more details). Similarly, in our analysis, we separate the gravity moments to the static gravity signal, which is due to the static density mass distribution of the planet and is calculated using an internal structure model, and the contribution from the dynamical density perturbations due to the zonal flows. Because our main goal is to determine the penetration depth of the observed zonal flows, we take these as a given and allow a wide range of penetration depths, which are the parameters we are trying to optimize.

2.1. The Thermal Wind Forward Model

Starting from the observed cloud-level winds, we first need to establish the nature of the subsurface flow. Since the planet is rapidly rotating, and Coriolis accelerations are dominant over the inertial accelerations (small Rossby number), surfaces of constant angular momentum will be nearly parallel to the axis of rotation (Kaspi et al. 2009; Schneider & Liu 2009).

Conservation of angular momentum then implies, to leading order, that the flow is mainly zonal, i.e., that any meridional circulation will be much weaker than the zonal flow. These zonal flows have been shown in numerical models to have a structure that is aligned with the axis of rotation, yet with wind speeds that decay with depth (Kaspi et al. 2009). Therefore, similar to Kaspi et al. (2010) we assume that the zonal wind field has the form

$$u(r, \theta) = u_0 \exp\left(\frac{r - a}{H}\right), \tag{2}$$

where $u_0(r, \theta)$ are the observed cloud-level zonal winds extended constantly along the direction of the axis of rotation, but here we allow the e-folding decay depth of the cloud-level wind, $H(\theta)$, to vary with latitude. This enables extra degrees of freedom in the possible structure of the winds compared to previous studies such as Kaspi et al. (2010), Kaspi (2013), and Liu et al. (2013). A latitudinal dependent decay depth can occur for several reasons, such as the internal convection extent varying with latitude (e.g., Aurnou et al. 2008), ohmic dissipation being latitudinally varying (Liu et al. 2008; Liu & Schneider 2010), moist convection having different latitudinal behavior (Lian & Showman 2010), or by different dynamics inside and outside the tangent cylinder surrounding the metallic hydrogen envelope (e.g., Heimpel & Aurnou 2007; Gastine et al. 2013; Heimpel et al. 2015). The latitude dependent H is defined as a summation over the first 20 Legendre polynomials

$$H(\theta) = \sum_{i=0}^{19} h_i P_i(\theta), \tag{3}$$

where h_i are the coefficients by which the shape of $H(\theta)$ is determined. Such a formulation allows for a solution to be found separately for different spatial scales of the winds and its resulting gravity signals. Note that, when setting $h_{i=1..19} = 0$, the depth of the winds is set to be constant with latitude. Since we expect the dynamics to be in the regime of small Rossby numbers, the flow to leading order is in geostrophic balance, and therefore thermal wind balance must hold so that

$$(2\Omega \cdot \nabla)[\tilde{\rho}\boldsymbol{u}] = \nabla\rho' \times \boldsymbol{g}_0, \tag{4}$$

where Ω is the planetary rotation rate, $\boldsymbol{u}(\boldsymbol{r})$ is the full 3D velocity, $\boldsymbol{g}_0(r)$ is the mean gravity vector,[1] and $\rho'(r, \theta)$ is the dynamical density anomaly (Pedlosky 1987; Kaspi et al. 2009). Here the thermal wind balance is written in a general form without making any assumptions on the depth of the circulation. The mean static density $\tilde{\rho}(r)$ and $\boldsymbol{g}_0(r)$ are calculated using the model of Hubbard (1999; see also Hubbard et al. 2014). Note that, in principle, the specific choice of these background fields affects the dynamical density anomalies; however, we found that using $\tilde{\rho}(r)$ and $\boldsymbol{g}_0(r)$ from different sources hardly affects the solution of the dynamical gravity field. Therefore, we consider $\tilde{\rho}(r)$ and $\boldsymbol{g}_0(r)$ as known parameters and do not try to optimize them.

[1] The gravity vector is calculated by integration of the static density $\tilde{\rho}$, and is therefore only a function of radius. Zhang et al. (2015) suggest a correction to this equation by adding a term associated with the nonradial component of the gravity vector due to dynamics. However, as also shown by the same authors, for the values of decay scale heights considered here and for gravity moments with $n > 2$, such a term is small.

Integrating the zonal component of Equation (4) latitudinally, the dynamical density $\rho'(r, \theta)$ can be calculated, and will depend only on the decay parameter $H(\theta)$ and a radially depending integration constant $\rho'_0(r)$, which, for small Rossby, numbers is small compared to the solid-body radial density profile, so that $\rho'_0 \ll \tilde{\rho}$ (Kaspi et al. 2013b). This integration constant, which physically represents a perturbation to the horizontal-mean radial density profile due to dynamics, does not contribute to the gravity field since it only depends on radius while the Legendre polynomials are only functions of latitude with a zero mean, and therefore do not contribute to the gravity moments in Equation (1). For this reason, calculations of the gravity signal using the thermal wind method as applied here are limited to spherical geometry. Then, the dynamically induced gravity moments due to the density anomaly ρ' are

$$\Delta J_n = -\frac{1}{Ma^n}\int_0^a r'^{n+2} dr' \int_0^{2\pi} d\phi' \times \int_{-1}^{1} P_n(\mu')\rho'(r', \mu') d\mu', \tag{5}$$

using spherical coordinates so that ϕ is longitude and $\mu = \cos\theta$. Note that unlike the dynamical gravity moments, the static gravity moments are dominated by the oblate shape of the planet, and therefore need to be calculated by other methods (e.g., Zharkov & Trubitsyn 1978; Hubbard 2012; Kong et al. 2012; Hubbard et al. 2014; Wisdom & Hubbard 2016).

In this study, we will simulate the gravity moments, but it is important to note that the resulting gravity signal itself, which can be estimated from radio tracking data, can then be calculated by taking the radial and latitudinal derivatives of the gravity potential $V(r) = 1 - \sum_{n=2}^{\infty}\left(\frac{a}{r}\right)^n J_n P_n(\mu)$ to give the radial and latitudinal components of the anomalous gravity perturbations due to wind given by

$$\delta g_r = g_0 \sum_{n=2}^{\infty}(n + 1)\lambda^n \Delta J_n P_n(\mu), \tag{6}$$

$$\delta g_\theta = g_0 \sum_{n=2}^{\infty}(1 - \mu^2)^{\frac{1}{2}}\lambda^n \Delta J_n \frac{dP_n}{d\mu}, \tag{7}$$

where g_0 is the mean surface gravity for the spherical planet, $\lambda = a/(a + r_p)$, and r_p is the local distance in the spacecraft's trajectory to the 1 bar surface. Note that for high moments this signal increases rapidly as the spacecraft is close to periapse.

In summary, given the observed cloud-level winds, and assuming a penetration depth of the winds and the dynamical balance between them and the density structure, we can calculate the resulting gravity perturbation on the planet surface. However, the problem we need to solve is the inverse one: given the gravity measurements, what would be the $H(\theta)$ that would best explain them. For that, we develop the adjoint model described in the next section.

2.2. The Adjoint Model

An efficient way to address the problem of determining the internal structure of the wind field, given the observations of the gravity moments J_n, a forward model such as that described above, and the observed cloud-level winds, is the adjoint method. This method allows for an effective optimization of

the model solution with respect to a cost function and control variables (e.g., Thacker & Long 1988; Tziperman & Thacker 1989; Tziperman 1992; Wunsch & Heimbach 2007; Mazloff et al. 2010). The adjoint method has been used extensively in geophysical fluid dynamics problems on Earth, both in the ocean (e.g., Marotzke et al. 1999; Galanti et al. 2003; Ferreira et al. 2005; Kalmikov & Heimbach 2014) and in the atmosphere (e.g., Moore et al. 2011; Blessing et al. 2014). It is used for sensitivity studies as well as for optimization of parameters and data assimilation.

The cost function is the physical quantity we wish to minimize. It can be a measure of the deviation of the model solution from the observations, or simply the model solution itself. The control variables can be any parameter or model variable that has an effect on the cost function. The adjoint model is then a backward run of the derivatives of the cost function with respect to the model variables, linearized over its solution from the forward integration, with the final solution of the adjoint model being the sensitivity of the cost function with respect to the control variables. This sensitivity can be studied by itself, or be used to direct the model toward a solution that minimizes the cost function. In this study, we will use the adjoint mainly for optimization, but also examine the adjoint sensitivities that enable us to evaluate the sensitivity of our solutions to the wind velocities at different depths.

The cost function is defined as the difference between the model calculated moments and those measured, and the control variable is the decay parameter $H(\theta)$. We define the cost function as

$$\mathcal{J} = \Delta J^T \cdot W \cdot \Delta J + \epsilon \sum_{i=0}^{19} h_i^2, \tag{8}$$

$$\Delta J = J^c - J^o, \tag{9}$$

where J^c is the N size calculated model solution, J^o are the observed gravity moments, and W is a matrix of size $N \times N$ with weights given to each moment (diagonal terms) and covariance between moments (off-diagonal terms). In general, the values of the weights are set as the inverse of the observational error covariance matrix (Finocchiaro & Iess 2010), but given the conceptual nature of this study, for simplicity, we set the weights to be $W_{ii} = 4 \times 10^{16}$ and zero elsewhere, representing simulated uncertainties of 5×10^{-9} (a value similar to the high moments, see more in Section 3). The second term in Equation (8), which is set to be much smaller than the first and controlled by the value of ϵ, acts as a constraint on the optimized solution demanding that the values of h_i be as small as possible as long as they do not affect substantially the first term, thus reduce the effect of the unphysical initial guess on the final solution. For example, if a certain h_i has a large value in the initial guess, but has little effect on the cost function, i.e., it has a small projection on the gravitational moments, the second term acts to reduce its value. On the other hand, if that h_i has a significant projection on the gravitational moments, and therefore on the cost function, its value will be optimized. This second term should only come into play once the cost function has been substantially reduced, otherwise it will dominate the optimization process and instead of minimizing the difference between the model gravitational moments and the observed ones, the values of all h_i will be reduced regardless of their contribution to the moments. It is, therefore, important to keep the second term very small compared to the initial value of the cost function (at least by two orders of magnitude) to allow a physical optimization of the problem. With that, the value of ϵ should also not be too small, otherwise it will have no effect on the optimization process. For each case presented here, the value of the parameter ϵ was set according to the initial value of the cost function, to keep the necessary ratio.

Our goal is to minimize the cost function, i.e., bring the model solution closer to the observed, and therefore we need to calculate its sensitivity to changes in the decay parameter $H(\theta)$. For simplicity, we start with a single H, so that the sensitivity is

$$\lambda(H) \equiv \frac{\partial \mathcal{J}(J^c)}{\partial H} \tag{10}$$

with the modeled moments formulated as a series of operators

$$J^c = F_1(F_2(F_3(H))), \tag{11}$$

where F_1 is the solution of Equation (5), F_2 is the solution of Equation (4), and F_3 the solution of the spherical structure of the wind Equation (2), which is a function of H.

Therefore, the model Jacobian matrices for the three equations can be written in the form (e.g., Marotzke et al. 1999)

$$\lambda(H) \equiv \frac{\partial \mathcal{J}(H)}{\partial H} = \left(\frac{\partial \mathcal{J}}{\partial J^c}\right)\left(\frac{\partial J^c}{\partial \boldsymbol{\rho}}\right)\left(\frac{\partial \boldsymbol{\rho}}{\partial \boldsymbol{u}}\right)\left(\frac{\partial \boldsymbol{u}}{\partial H}\right). \tag{12}$$

Taking the transpose results in matrix-vector multiplications we get

$$\lambda^T \equiv \left(\frac{\partial L}{\partial H}\right)^T = \left(\frac{\partial \boldsymbol{u}}{\partial H}\right)^T \left(\frac{\partial \boldsymbol{\rho}}{\partial \boldsymbol{u}}\right)^T \left(\frac{\partial J^c}{\partial \rho}\right)^T \left(\frac{\partial \mathcal{J}}{\partial J^c}\right)^T, \tag{13}$$

which is the adjoint model to be used.

The solution of the adjoint model λ^T is the sensitivity of the cost function to a perturbation in the control variable H. Modifying the control variable iteratively according to the adjoint solution will result in a minimization of the cost function. In the case of a latitudinal dependent wind depth, where $H(\theta)$ is a function of the coefficients h_i, the adjoint solution has the form

$$\lambda_i^T \equiv \left(\frac{\partial \mathcal{J}}{\partial h_i}\right)^T = \left(\frac{\partial \boldsymbol{H}}{\partial h_i}\right)^T \left(\frac{\partial \boldsymbol{u}}{\partial H}\right)^T \left(\frac{\partial \boldsymbol{\rho}}{\partial \boldsymbol{u}}\right)^T \times \left(\frac{\partial \Delta J^c}{\partial \rho}\right)^T \left(\frac{\partial \mathcal{J}}{\partial \Delta J^c}\right)^T + 2\epsilon h_i, \tag{14}$$

where λ_i^T is the adjoint sensitivity with respect to the ith coefficient of Equation (3). Alternatively, the adjoint sensitivities could be formulated using Lagrange multipliers (e.g., Thacker & Long 1988; Tziperman & Thacker 1989). A detailed example on how the adjoint model is derived using the Lagrange multipliers is given in the Appendix.

The effectiveness of the adjoint method comes from its ability to provide the sensitivity to all control variables (in our case, h_i) in a single run of the forward and backward models. Having the adjoint solution, we can now proceed to construct the optimization of the model solution.

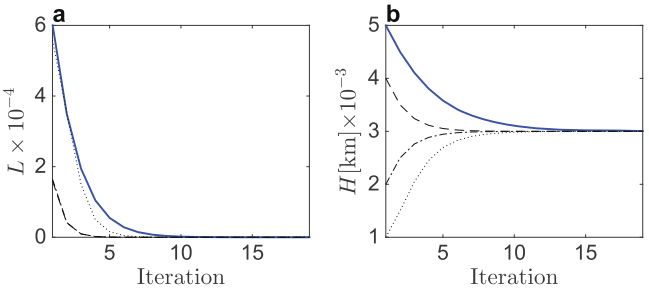

Figure 2. Example of the adjoint optimization. (a) The reduction of the cost function with iterations and (b) the change in the penetration depth as function of iterations. The solid line is for the optimization starting from an initial guess of $H = 5000$ km, while the other lines show the same optimization, but with the initial guess being $H = 4000$ km, $H = 2000$ km, and $H = 1000$ km. In all cases, the same solution is reached. Note that due to the nonlinear nature of the problem the convergence rate is different for the cases with initial guesses of $H = 5000$ km and $H = 1000$ km, even though they begin at the same distance from the solution. Also note that the dashed and dashed–dotted lines in (a) overlap.

2.3. Optimization Procedure

Once the gradient of the cost function λ is obtained, the control variables (either a single depth H, or coefficients h_i) are modified so that in the next iteration the cost function will have a lower value. In the case of a single H, there is only one option to change the control variable—in the direction opposite to the value of the adjoint solution. In the case of optimizing h_i, moving directly (steepest descent) is not efficient, therefore, a conjugate gradient method is applied so that the direction of modifying the control variables is the optimal one (Hestenes 1980). The extent of the change is also controlled using a line search (Hestenes 1980), so that the change in the control variable does not cause the cost function to move beyond the global minimum. The global minimum is defined to be reached when each of the gravitational moments is as close to the value of the observed one as the size of the uncertainty assigned to it. Therefore, after each iteration, we check the value of each element in ΔJ to see whether it is small compared to the observational uncertainty (in our case, 5×10^{-9}), and if all of the calculated moments are within this uncertainty the optimization is complete. At the final iteration, the Hessian matrix C (second derivative of the cost function) is calculated in order to estimate the uncertainties associated with each control variable (Tziperman & Thacker 1989). Inverting the Hessian matrix C, we get the error covariance matrix G. Finally, the cross-correlated uncertainties G_{ij} are projected into the physical space of H, and are used as formal bounds on the solution. Note that if the control variable is a single depth H, the size of the Hessian matrix is 1×1. The adjoint optimization was tested with various wind depths, and is found to be able to reach a solution within 10 to 60 iterations (see the examples in Figures 2 and 3). In addition, an important criteria for the robustness of the solution is whether the minimum reached is global, i.e., would the same solution be reached if starting from different initial guesses? In order to test this, we tested each of the experiments presented in this study, starting from different initial guesses and checking if the same solution is reached. An example of such a test is shown in Figure 2, where the different curves show the optimization process for different initial guesses. We found that in all experiments discussed in Section 3 the adjoint optimization is insensitive to the choice of the initial guess—the same solution is being reached regardless of the initial guess, only the number of iterations needed might change. Therefore, we conclude that the global minimum of the problem is indeed being reached and the method is valid for the problems presented.

3. RESULTS

We now show how the adjoint method is used to produce a wind structure, given the surface wind velocities and a set of gravity moments. In all cases presented below, the following approach was taken. First, the forward model was run with a chosen depth of winds and the gravitational moments were calculated. These moments are then defined as the *simulation*. This solution is used to mimic the upcoming *Juno* or *Cassini* observations. In order to allow for observational errors, a uniformly distributed error with a magnitude of 5×10^{-9} is added to the gravity moments. This value corresponds to the average error measurement we expect for lowest order moments (Finocchiaro & Iess 2010). Second, the adjoint optimization is used to find the *solution* closest to the simulated moments, starting from an *initial guess* and then searching for the solution using the optimization procedure.

3.1. Inversion of the Gravity Signal

We start with a Jupiter case, where first, for simplicity, the observed winds of Jupiter are set to penetrate to the same depth in all latitudes. Therefore, the adjoint optimization is trying to minimize the cost function with respect to a single depth H. The simulation is done with $H = 3000$ km, and the initial guess

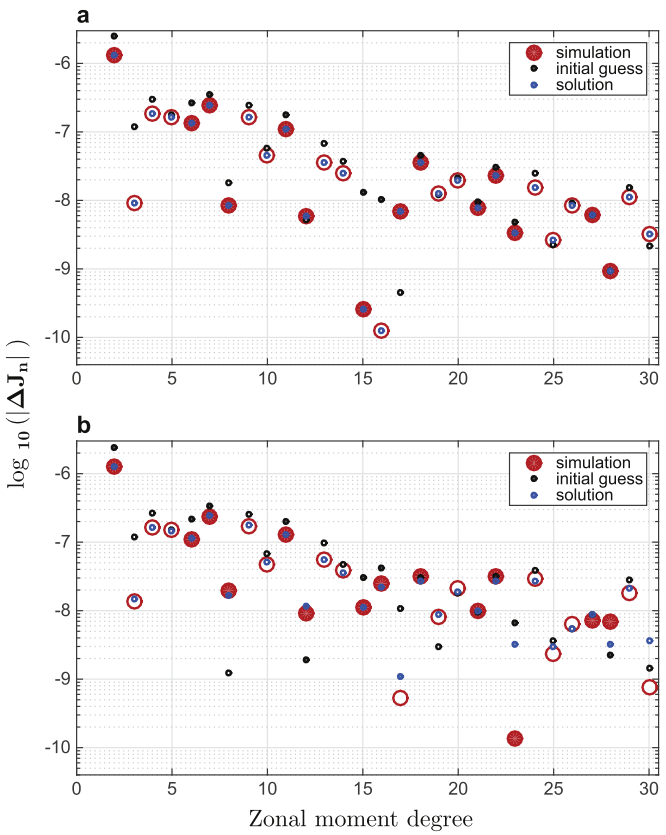

Figure 3. Jupiter gravitational moments for (a) a case with no errors in the simulated moments, and (b) a case with random errors. Shown are the simulation (red), initial guess (black), and solution (blue). Filled (open) circles denote positive (negative) values.

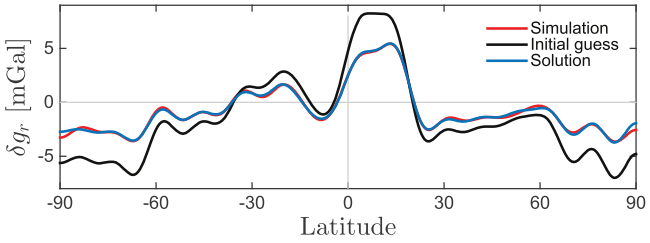

Figure 4. Case with simulated $H = 3000$ km and the initial guess $H = 5000$ km. Shown are the radial component of the gravitational anomalies (in mGals), as a function of latitude, for the simulation (red), the initial guess (black), and the solution (blue).

was set to $H = 5000$ km. The progression of the adjoint optimization is shown in Figure 2 (solid lines). It can be seen that the within five iterations the cost function value is reduced by an order of magnitude, and the calculated wind depth is getting closer to the simulated one. The gravitational moments for the simulation, initial guess, and solution are shown in Figure 3 for a case without errors in the simulated moments (panel (a)) and for a case with errors (panel (b)). While, in the former case, the moments reach a perfect fit to the simulation, in the latter case, the lower moments are fitted well and the higher moments are less so, since the errors applied to the simulation have a relatively larger effect on the higher moments, which are smaller.

The gravitational moments can be transformed into the actual latitudinal dependent gravity anomalies (Equation (6)). The radial component of these anomalies, calculated at the planet's 1 bar level, are shown in Figure 4, for the adjoint solution, together with the simulation and initial guess. Note that as a result of the complex surface wind structure (Figure 1), even with a single H the resulting gravity field has a pronounced asymmetry between the northern and southern hemispheres. While the initial guess differs considerably from the simulation, the solution matches the simulation well. The difference between the simulation and the solution is a result of the errors we apply to the simulation. In a case with no random errors the solution is identical to the simulation (not shown). Given the good agreement between the adjoint solution and the simulation, it is clear that most of the gravity signal is contained in the lower moments. Note that the differences in the moments (Figure 3) have only a minor effect on the actual gravity field; therefore, for the next more complicated cases, we show the gravity field and not the gravitational moments.

Next, the wind penetration depth is allowed to vary with latitude. In this case, the adjoint optimization is trying to minimize the cost function with respect to the set of coefficients h_i. The simulation was done with an $H(\theta)$ that is deeper at the equator and shallower toward the poles, representing possibly deeper dynamics outside of the tangent cylinder (Aurnou et al. 2007), where drag might be playing a lesser role (Liu & Schneider 2010). The simulation $H(\theta)$ has an asymmetry between the hemispheres, and the initial guess was chosen to reflect a complex dependence on latitude (Figure 5(b)). The adjoint solution over most latitudes (see below) is in good agreement with the simulation, in both the gravity anomalies (Figure 5(a)) and the depth of the winds (Figure 5(b)).

The adjoint model also gives us the ability to rigorously estimate the uncertainty associated with the solution. This is done by calculating the Hessian matrix and from that the error covariance matrix (Figures 6(a) and (b), respectively). The Hessian matrix gives an estimate to the sensitivity of the cost function to cross perturbations in the control variables; the higher the value, the better our ability to determine the values of these parameters. Inverting the Hessian matrix reveals the covariance of the uncertainties associated with each control variable (Figure 6(b)). The highest uncertainties are in the diagonal terms of the higher coefficients, meaning that the coefficients are not significantly affecting each other, and that most of the uncertainties are in the spatially highly variable features (higher moments). In order to further verify this, the covariance matrix can be used to calculate the uncertainty in H at each latitude using

$$\epsilon_H(\theta) = \sqrt{\sum P_i(\theta) P_j(\theta) G_{ij}} \tag{15}$$

where G_{ij} are the cross-correlations between the coefficients h_i and h_j, and $P_i(\theta)$ is the Legendre polynomial at latitude θ. The uncertainty in H (Figure 6(c)), is found to be largest near the poles since this is where the winds are weakest. This uncertainty is also plotted in Figure 6(b) to illustrate the usefulness of the solution for H. It is clear that where the uncertainty in H is small, the solution matches the simulation well (low latitudes), and, where the uncertainty is large, the solution deviates considerably from the simulation (high latitudes). This has implications for the expected usefulness of the upcoming gravitational measurements by *Juno* and *Cassini* in determining the depth of the winds on both Jupiter and Saturn. Even in a case where the uncertainties of the measured gravity field are very small, due to the weak wind close to the poles it will not be possible to determine with certainty the depth of the flow in the polar regions. Moreover, the planned periapses of the orbit of both *Juno* and *Cassini* are at low latitudes, meaning that the sensitivity to higher latitude induced signals will be smaller (Finocchiaro & Iess 2010; Finocchiaro 2013).

Next, we repeat the experiment for Saturn. The main difference between the planets, aside from the different physical parameters, is in the surface wind pattern (Sanchez-

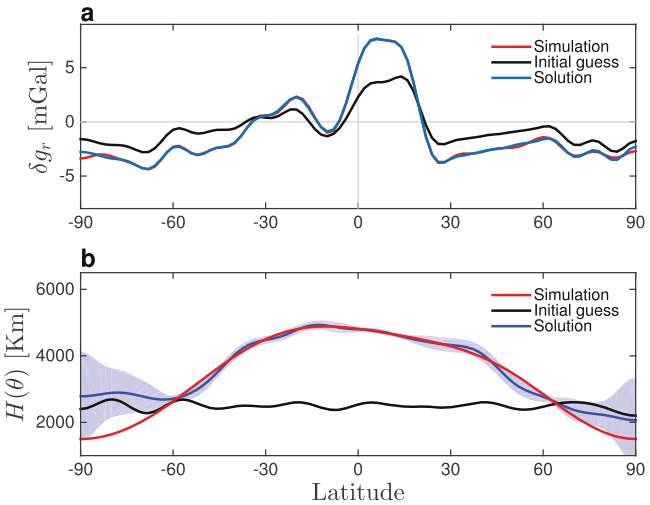

Figure 5. Case with latitudinal dependent decay depth $H(\theta)$. (a) The gravitational anomalies (in mGals) as a function of latitude, and (b) the depth of the winds. Shown are the simulation (red), initial guess (black), and solution (blue). For the solution of the wind depth, also shown are the associated uncertainties (blue shading).

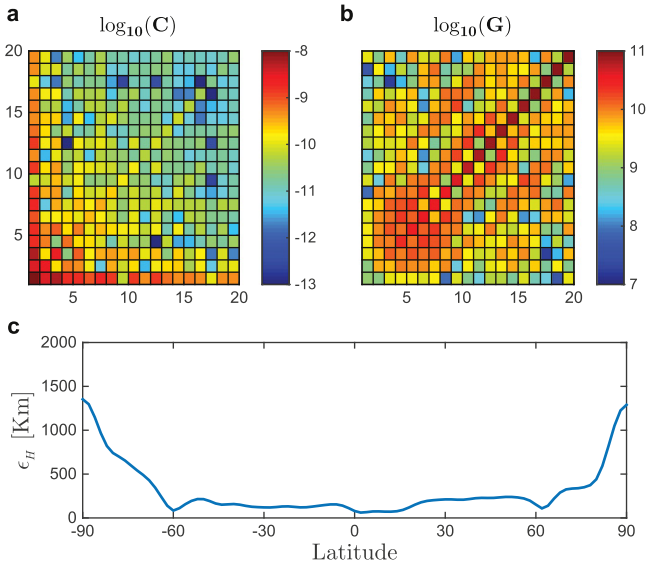

Figure 6. (a) Hessian matrix associated with the adjoint solution. (b) The error covariance matrix. (c) The uncertainties in the solution for the depth of the winds, as calculated from the diagonal of the error covariance.

Lavega et al. 2000, 2007; Garcia-Melendo et al. 2011). While, on Jupiter, the winds vary considerably with latitude, on Saturn, the much stronger winds have a simpler latitudinal pattern (Figure 1). As in the case of Jupiter, the simulation was done with H that is deeper at the equator and shallower toward the poles, with an asymmetry between the hemispheres; the initial guess was chosen to reflect a complex dependence on latitude (Figure 7(b)). Since the shape of the surface winds are much different in the Saturn case, the resulting gravity anomalies are also very different (Figure 7(a)). Still, similarly to the Jupiter case, the solution matches closely the simulation in the low latitudes and less so closer to the poles. This characteristic is evident in the associated uncertainties, shown in Figure 7(b) as the shaded area around the solution.

3.2. Changing the Physical Assumptions

Thus far, we have used the same physical assumptions in both the model used for calculating the "simulation" and the model used to find the "solution." However, a valid question is how well the adjoint optimization would work when the model used to find the solution is different from the one used for generating the simulation—in reality, we should expect that any model used to interpret *Juno* observations will lack some of the physics embedded in the observations.

In order to get insight into the matter, we examine two cases in which the model used for optimization differs from that used for the simulation. First, we set the "simulation" with the depth of the wind being constant with latitude, and ask the optimization to look for a depth that varies with latitude (Figure 8). The simulation was done with $H = 4000$ km, the initial guess was set with depths of winds that vary between 3000 km near the equator and 1000 km near the poles. The optimized solution follows the simulated depth closely, aside from the polar regions, where it deviate by about 1000 km (as expected from its uncertainties). This experiment challenges the optimization more than the previous ones, but is still within the framework of the physical model used for both simulation and optimization, since we can view the simulation as done with latitude, varying depth set with Equation (3) with $h_0 = 4000$ km and $h_{1-19} = 0$.

A more challenging setup can be done by generating the simulation with a latitude varying depth and looking for a solution in which the depth of the wind is assumed to be constant with latitude. In such a case, we can expect that the simulated solution could not be reached, since the physical model used in the optimization lacks some of the physics used in the simulation. We set the experiment with the simulation based on the same depth distribution as in the previous section, and set the initial guess to be $H = 2000$ km (Figure 9). As expected, it can be seen that the solution $H = 4327$ km does not match the simulated one, yet it is in the proximity of the wind depth in the equatorial region. Moreover, looking at the actual gravity field (Figure 9(a)), the solution captures most of the signal contained in the simulation, especially in the low and mid-latitudes.

The two experiments discussed here show that the adjoint method can deal with cases in which the physical assumptions regarding the depth of the wind used in the optimization differ from those used in the simulation. In the next section, we discuss the sensitivity of the solution to deep flow patterns, an additional complication.

3.3. Sensitivity to Deep Wind Patterns

Aside from the question of how deep the cloud-level winds penetrate, it might also be the case that a different structure of flow exists in the interior, that does not have any signature at the observed cloud-level wind. Because deeper levels have more mass, it is possible that the measured gravity signal will come from these levels (Galanti & Kaspi 2015). As long as this flow structure is large scale it will also likely be geostrophic and, therefore, in thermal wind balance with an associated density modulation that will affect the gravity field. Using the adjoint method, we can get an estimate on the sensitivity of the cost function to perturbations in the two-dimensional wind field, regardless of the surface winds. In fact, this can be also

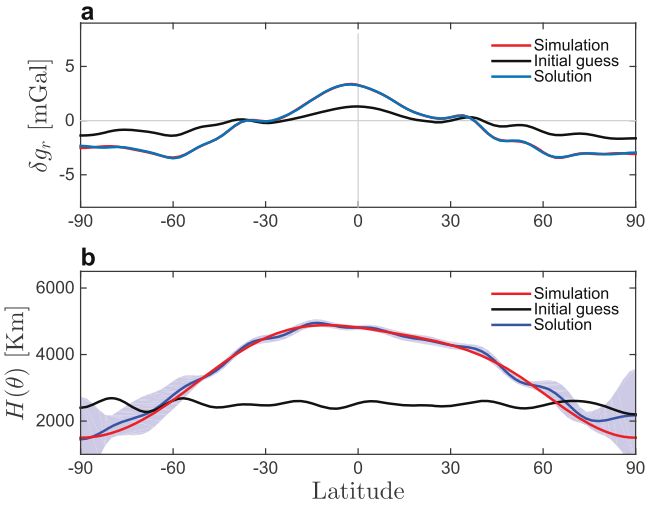

Figure 7. (a) The Saturn gravitational anomalies (in mGals) as a function of latitude, and (b) the depth of the winds. Shown are the simulation (red), initial guess (black), and solution (blue). For the solution of the wind depth, also shown are the associated uncertainties (blue shadow).

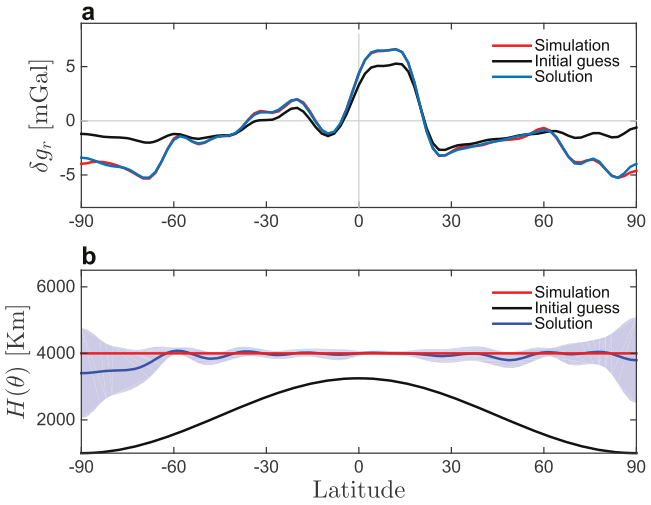

Figure 8. Case where the simulated wind depth is constant with latitude and the solution varies with latitude. (a) Jupiter gravitational anomalies (in mGals) as function of latitude, and (b) the depth of the winds. Shown are the simulation (red), initial guess (black), and solution (blue). For the solution of the wind depth, also shown are the associated uncertainties (blue shadow).

done in 3D, using the Tesseral moments (Parisi et al. 2016), but because the aim of this study is to present this method, we keep the analysis simple with just the 2D (zonally averaged) wind fields. To perform this estimate, the forward model was run with a wind depth of 5000 km (this choice does not affect the solution, aside from some minor nonlinear contributions). Defining the cost function to be the sum of the square of the gravitational moments

$$\mathcal{J} = \sum_n W_n (J_n^c)^2, \tag{16}$$

the adjoint model is integrated to produce the adjoint sensitivities, which are the sensitivity of the cost function to any of the model prognostic variables. In our case, they include the gravitational moments, the density perturbations, the wind structure, and the depth parameter (see Equation (13)). The value of the sensitivities is the change in the cost function expected when perturbing the variable with a unit change.

We then save the adjoint variables of both the density and wind,

$$\lambda_\rho(z,\theta) \equiv \left(\frac{\partial J^c}{\partial \rho}\right)^T \left(\frac{\partial \mathcal{J}}{\partial \Delta J^c}\right)^T,$$
$$\lambda_U(z,\theta) \equiv \left(\frac{\partial \boldsymbol{\rho}}{\partial \boldsymbol{u}}\right)^T \left(\frac{\partial J^c}{\partial \rho}\right)^T \left(\frac{\partial \mathcal{J}}{\partial J^c}\right)^T, \tag{17}$$

which are a function of latitude and depth. The adjoint solution for the sensitivity to the density and wind is specific to the model's numerical structure in general, and to the grid structure in particular. Given that the grid in the model is not regular, i.e., the size of the grid box changes with depth, the adjoint solution needs to be normalized by the size of the grid box in order to show the physical sensitivity. Figure 10 shows the normalized sensitivities to density perturbations and wind perturbations. While the sensitivities to the density mostly bears the shape of J_2, and are highest close to the surface (due to the strong dependence of the gravitational moments on the distance from the surface), the sensitivities to the zonal velocity show a different structure. There exists a single pattern of positive sensitivities, located close to the equator, with the maximum around a depth of 10,000 km from the surface. The sensitivities decay gradually toward high latitudes. This is due to the nature of the thermal wind balance, in which the vertical gradient of the density is a function of the latitudinal gradient of the wind, so that a wind perturbation at a certain depth will imply a density perturbation from that depth to the surface. This implies that the highest sensitivities to deep winds, if they exist, will be to winds at the range of ~10,000 km below the cloud level and limited to low latitudes. The possibility that deep flows exist separately from the surface wind and their affect on the gravity field must be further examined in future studies.

4. DISCUSSION AND CONCLUSION

Modern observations of the gas giants since the 1970s have allowed these planets to be studied in great detail, particularly regarding processes at their cloud level. However, much of the processes controlling the levels below have remained unknown mainly due to the lack of observational data. This will likely change in the coming few years as the upcoming *Juno* mission and *Cassini* proximal orbits bring the possibility of investigating the sub-cloud levels in detail with several different instruments. Particularly, radio measurements will provide high-precision gravity soundings, i.e., data that can be used to estimate the depth of the observed surface flows on these planets. All models to date, relating the winds to the gravity field, have been in the forward direction, thus allowing only a calculation of the gravity field from a given wind model. Here, we propose a method to solve the inverse problem of deriving the depth of the winds from the gravity data. We use an adjoint based inverse dynamical model to relate the expected measurable gravity field, to perturbations of the density and wind fields, and therefore to the observed cloud-level winds. In order to invert the gravity field to be measured by *Juno* and *Cassini* into the circulation, an adjoint model is constructed for the dynamical model, thus allowing backward integration of the thermal wind model.

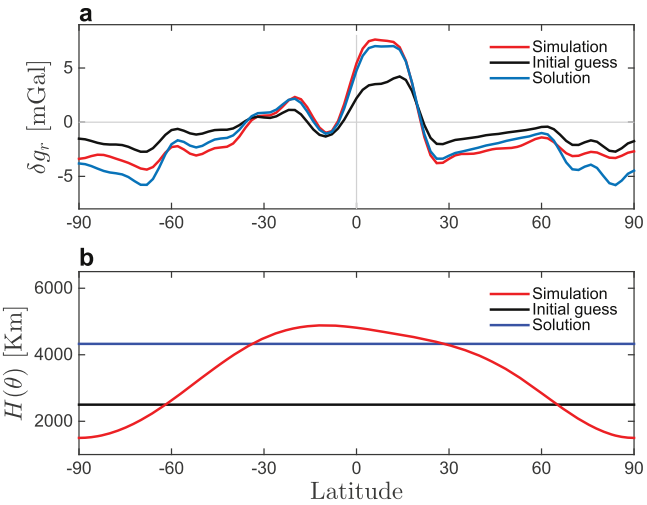

Figure 9. Case where the simulated wind depth varies with latitude, but the solution has a constant depth. (a) Jupiter gravitational anomalies (in mGals) as a function of latitude, and (b) the depth of the winds. Shown are the simulation (red), initial guess (black), and solution (blue).

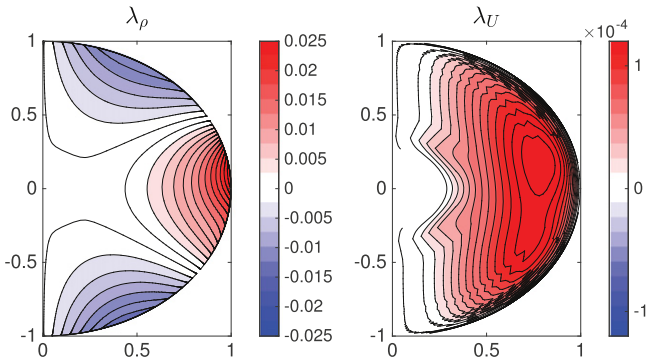

Figure 10. Sensitivity of the cost function to perturbations in ρ (left) and U (right).

The thermal wind method allows perhaps the simplest relation between the flow velocity and the dynamically balanced density gradients, which can be then related to the gravity field. Therefore, we have applied the adjoint method to the thermal wind model; however, the methodology presented here is not specific to this model and could be used to study and optimize any type of model, ranging from simple conceptual models to complex general circulation models (e.g., Marotzke et al. 1999; Galanti et al. 2003; Mazloff et al. 2010). In any such model, the adjoint method will allow for the backward calculation of the flow field that best matches the measured gravity field. Models with more complex physics will allow the inclusion of processes not taken into account here such as magnetic effects, internal convection, etc. Nonetheless, as long as the large-scale motion on these planets is controlled to leading order by the rotation of the planet, even models containing more physical processes would be to leading order in thermal wind balance. Therefore, this analysis captures the leading order dynamical balance between the gravity and the winds. More sophisticated wind structures with more complex depth and latitudinal dependencies, and weaker coupling to the cloud-level wind can also be considered.

This tool proves to be useful for various scenarios, simulating cases in which the depth of the wind is constant, or varies with latitude. We show that it is possible to use the gravity measurements to derive the depth of the winds, both on Jupiter and Saturn, also taking into account measurement errors. We find that due to the winds on both planets being much stronger in the equatorial regions, the model solutions are better determined in the low to mid-latitudes, while the depth of the winds close to the poles cannot be determined with good accuracy. Comparing Jupiter and Saturn, it is found that the latitudinal shape of the winds considerably affects the gravity field. The adjoint method also shows which regions of the planet have the highest impact on the gravity field. We find that the gravitational moments are most sensitive to winds at depths of around 10,000 km, especially at the equatorial region, but the signature of deep flows will appear in the gravity field even if the flows are much shallower. Therefore, if deep winds exist on these planets, they will likely leave a measurable signature on upcoming measurements.

We thank the *Juno* science team, Eli Tziperman, and Adam Showman for useful discussions and comments. This research has been supported by the Israeli ministry of Science under grants 3-11481 and 45-851-641, and the Helen Kimmel Center for Planetary Science at the Weizmann Institute of Science.

APPENDIX
AN EXAMPLE OF THE DERIVATION OF THE ADJOINT MODEL

In order to give a better understanding of the adjoint method, we illustrate the derivation of the adjoint equations for a simple case. The same principle could be applied to any set of partial differential equations (see another example in Tziperman & Thacker 1989). Consider a simple one-dimensional advection-diffusion equation in steady state for a tracer $c(x)$

$$uc_x = kc_{xx}, \tag{18}$$

where the parameters we wish to optimize are u and k (the parameters in this example are equivalent to the depth of the wind in our experiments, and the tracer is equivalent to the density or velocity fields). We set the two boundary conditions as

$$\begin{aligned} uc - kc_x|_{x=0} &= F_0, \\ uc - kc_x|_{x=L} &= F_L. \end{aligned} \tag{19}$$

The cost function is set to be the difference between the calculated tracer c and the observed tracer $c^{\rm obs}$

$$\mathcal{J} = \frac{1}{2}\int_0^L (c(x) - c^{\rm obs}(x))^2 dx.$$

Next, we define a Langrange function to include the constraints due to the dynamical Equation (18)

$$\mathcal{L} = \mathcal{J} + \int_0^L \lambda(uc_x - kc_{xx})dx, \tag{20}$$

where λ is the Lagrange multiplier that will turn out to be the adjoint variable for the tracer c. Because the second term is identically zero, the values of $\mathcal{L}$ and $\mathcal{J}$ are equal. The minimum of the cost function $\mathcal{J}$ (model solution) is reached when the Langrange function $\mathcal{L}$ has an extremum (zero derivative). Consider an arbitrary variation in the function c,

$$\begin{aligned} \delta\mathcal{L} = L(c+\delta c) - \mathcal{L}(c) = &\int_0^L (c(x) - c^{\rm obs}(x))\delta c dx \\ &+ \int_0^L \lambda(u\delta c_x - k\delta c_{xx})dx, \end{aligned} \tag{21}$$

where δc is an infinitesimally small arbitrary function in x, aside from the boundaries where it must conform to the boundary conditions (see the details below). Applying integration by parts, we get

$$\begin{aligned} \delta\mathcal{L} = &\int_0^L [c(x) - c^{\rm obs}(x) - (u\lambda_x + k\lambda_{xx})]\delta c dx \\ &+ \lambda[u\delta c - k\delta c_x]_{x=0}^L + \delta c[k\lambda_x]_{x=0}^L. \end{aligned} \tag{22}$$

Now, we need two conditions under which $\delta\mathcal{L}$ is zero. The second line in Equation (22) has exactly the formulation of the boundary conditions stated above, but for the variation δc. Since the boundary conditions should not change with variations in c, this term is zero by definition. Next, we can demand that the third line vanishes for any δc, i.e., that the boundary conditions for the adjoint variable λ are $[k\lambda_x]_{x=0}^L = 0$. We can do so because λ is not a physical variable so its boundary conditions could be set to fit the requirement on $\mathcal{L}$. Finally, we demand that $\delta\mathcal{L}$ is zero for any function δc; therefore, the integrand in the first line of

Equation (22) must vanish, which gives an equation for the adjoint variable λ

$$u\lambda_x + k\lambda_{xx} = c(x) - c^{\rm obs}(x). \quad (23)$$

Finally, once we have the formulation for the adjoint variable λ, we can optimize the cost function with respect to the parameters u and k. The derivative of the cost function with respect to these two parameters could be easily found by the differentiation of Equation (20) with respect to the two variables, so that

$$\frac{\partial \mathcal{L}}{\partial u} = \int_0^L \lambda c_x dx, \qquad \frac{\partial \mathcal{L}}{\partial k} = -\int_0^L \lambda c_{xx} dx. \quad (24)$$

Thus, calculating λ (the sensitivity of the cost function with respect to the tracer c), and then integrating using Equation (24), we can find the gradient of the cost function with respect to the control variables, i.e., the direction in which those parameters should be changed in order to reach the minimum of the cost function. Note that the control variables should be modified in the direction opposite the adjoint solution. Given that solving this example, and the actual model described in this study, needs to be done numerically, it is important that the adjoint model is actually derived from the finite difference formulation of the forward model, and not from the analytical version. The adjoint of the finite difference was shown to be more accurate than the finite difference of the adjoint (Sirkes & Tziperman 1997).

REFERENCES

Atkinson, D. H., Pollack, J. B., & Seiff, A. 1996, Sci, 272, 842
Aurnou, J., Heimpel, M., Allen, L., King, E., & Wicht, J. 2008, GeoJI, 173, 793
Aurnou, J., Heimpel, M., & Wicht, J. 2007, Icar, 190, 110
Blessing, S., Kaminski, T., Lunkeit, F., et al. 2014, TellA, 66, 22606
Bolton, S. J. 2005, Juno Final Concept Study Report Tech. Rep. AO-03-OSS-03 (New Frontiers, NASA)
Busse, F. H. 1976, Icar, 29, 255
Cho, J., & Polvani, L. M. 1996, PhFl, 8, 1531
Del Genio, A., & Barbara, J. 2012, Icar, 219, 689
Ferreira, D., Marshall, J., & Heimbach, P. 2005, JPO, 35, 1891
Finocchiaro, S. 2013, PhD thesis, Pubblicazioni Aperte Digitali della Sapienza
Finocchiaro, S., & Iess, L. 2010, Spaceflight Mechanics, 136, 1417
Galanti, E., & Kaspi, Y. 2015, in AAS/47th Division for Planetary Sciences Meeting Abstracts, 403.08
Galanti, E., Tziperman, E., Harrison, M., Rosati, A., & Sirkes, Z. 2003, MWRv, 131, 2748
Garcia-Melendo, E., Perez-Hoyos, S., Sanchez-Lavega, A., & Hueso, R. 2011, Icar, 215, 62
Gastine, T., Wicht, J., & Aurnou, J. M. 2013, Icar, 225, 156
Heimpel, M., & Aurnou, J. 2007, Icar, 187, 540
Heimpel, M., Gastine, T., & Wicht, J. 2015, NatGe, 9, 19
Hestenes, M. 1980, Conjugate Direction Methods in Optimization (Berlin: Springer-Verlag)
Hubbard, W. 1982, Icar, 52, 509
Hubbard, W. B. 1984, in Planetary Interiors (New York: Van Nostrand Reinhold Co.), 334
Hubbard, W. B. 1999, Icar, 137, 357
Hubbard, W. B. 2012, ApJL, 756, L15
Hubbard, W. B. 2013, ApJ, 768, 43
Hubbard, W. B., Schubert, G., Kong, D., & Zhang, K. 2014, Icar, 242, 138
Kalmikov, A., & Heimbach, P. 2014, SIAM Journal on Scientific Computing, 36, S267
Kaspi, Y. 2013, GeoRL, 40, 676
Kaspi, Y., Davighi, J., Galanti, E., & Hubbard, W. 2013a, in AGU Fall Meeting Abstracts P21C-1740
Kaspi, Y., Davighi, J. E., Galanti, E., & Hubbard, W. B. 2016, Icar, submitted
Kaspi, Y., & Flierl, G. R. 2007, JAtS, 64, 3177
Kaspi, Y., Flierl, G. R., & Showman, A. P. 2009, Icar, 202, 525
Kaspi, Y., Hubbard, W. B., Showman, A. P., & Flierl, G. R 2010, GeoRL, 37, L01204
Kaspi, Y., Showman, A. P., Hubbard, W. B., Aharonson, O., & Helled, R. 2013b, Natur, 497, 344
Kong, D., Zhang, K., & Schubert, G. 2012, ApJ, 748, 143
Li, L., Ingersoll, A., Vasavada, A., et al. 2006, JGRE, 111, 4004
Lian, Y., & Showman, A. P. 2010, Icar, 207, 373
Liu, J., Goldreich, P. M., & Stevenson, D. J. 2008, Icar, 196, 653
Liu, J., & Schneider, T. 2010, JAtS, 67, 3652
Liu, J., Schneider, T., & Fletcher, L. N. 2014, Icar, 239, 260
Liu, J., Schneider, T., & Kaspi, Y. 2013, Icar, 224, 114
Marotzke, J., Giering, R., Zhang, K., et al. 1999, JGRC, 104, 29529
Mazloff, M. R., Heimbach, P., & Wunsch, C. 2010, JPO, 40, 880
Moore, A. M., Arango, H. G., Broquet, G., et al. 2011, PrOce, 91, 34
Parisi, M., Galanti, E., Finocchiaro, S., Iess, L., & Kaspi, Y. 2016, Icar, 267, 232
Pedlosky, J. 1987, Geophysical Fluid Dynamics (Berlin: Spinger)
Porco, C. C., West, R. A., McEwen, A., et al. 2003, Sci, 299, 1541
Sanchez-Lavega, A., Hueso, R., & Perez-Hoyos, S. 2007, Icar, 187, 510
Sanchez-Lavega, A., Rojas, J. F., & Sada, P. V. 2000, Icar, 147, 405
Schneider, T., & Liu, J. 2009, JAtS, 66, 579
Scott, R. K., & Polvani, L. M. 2007, JAtS, 64, 3158
Showman, A. P., Gierasch, P. J., & Lian, Y. 2006, Icar, 182, 513
Sirkes, Z., & Tziperman, E. 1997, MWRv, 125, 3373
Thacker, W., & Long, R. 1988, JGRC, 93, 1227
Tziperman, E. 1992, DyAtO, 16, 379
Tziperman, E., & Thacker, W. C. 1989, JPO, 19, 1471
Vasavada, A. R., & Showman, A. P. 2005, RPPh, 68, 1935
Williams, G. P. 1978, JAtS, 35, 1399
Wisdom, J., & Hubbard, W. 2016, Icar, 267, 315
Wunsch, C., & Heimbach, P. 2007, PhyD, 230, 197
Zhang, K., Kong, D., & Schubert, G. 2015, ApJ, 806, 270
Zharkov, V. N., & Trubitsyn, V. P. 1978, Physics of Planetary Interiors (Chichester: Pachart Publishing House)